

# Polarimetry toward the *IRAS* Vela Shell. II. Extinction and Magnetic Fields

A. Pereyra and A. M. Magalhães

*Departamento de Astronomia, IAG, Universidade de São Paulo, Rua do Matão 1226, São Paulo, SP, 05508-900, Brazil*

antonio@astro.iag.usp.br

## ABSTRACT

We explore correlations between visual extinction and polarization along the western side of the *IRAS* Vela Shell using a published polarimetric catalog of several hundreds of objects. Our extinction maps along this ionization front (I-front) find evidence of clumpy structure with typical masses between 1.5 and 6  $M_{\odot}$  and a mean length scale  $L \sim 0.47$  pc. The polarimetric data allowed us to investigate the distribution of the local magnetic field in small ( $\sim$ pc) scales across the I-front. Using the dispersion of polarization position angles, we find variations in the kinetic-to-magnetic energy density ratio of, at least, one order of magnitude along the I-front, with the magnetic pressure generally dominating over the turbulent motions. These findings suggest that the magnetic component has a significant contribution to the dynamical balance of this region. Along the I-front, the mean magnetic field projected on the sky is  $[0.018 \pm 0.013]$  mG. The polarization efficiency seems to change along the I-front. We attribute high polarization efficiencies in regions of relatively low extinction to an optimum degree of grain alignment. Analysis of the mass-to-magnetic flux ratio shows that this quantity is consistent with the subcritical regime ( $\lambda < 1$ ), showing that magnetic support is indeed important in the region. Our data extend the overall  $\lambda-N(\text{H}_2)$  relation toward lower density values and show that such trend continues smoothly toward low  $N(\text{H}_2)$  values. This provides general support for the evolution of initially subcritical clouds to an eventual supercritical stage.

*Subject headings:* polarization — ISM: clouds — ISM: individual (Gum Nebula, Vela Shell) — ISM: extinction — ISM: magnetic fields

## 1. Introduction

Magnetic fields are important for the dynamics of expanding shells (Spitzer 1978; Troland & Heiles 1982; Draine & McKee 1993). Models of the interaction of shocks and ionization fronts in shells with magnetic fields exist in several configurations and media (Hartquist, Pilipp, & Havnes 1997; Pilipp, Hartquist, & Havnes 1990; Pilipp & Hartquist 1994; Redman et al. 1998; Wardle 1998; Williams, Dyson & Hartquist 2000; Williams & Dyson 2001). A proper determination of the magnetic field in shells is necessary to constraint these models.

Following Chandrasekhar & Fermi (1953, hereinafter CF), the dispersion of polarization position angles, observed through a polarizing medium, permits to estimate the strength of the magnetic field component in the plane of the sky ( $B$ ). In addition, this dispersion also yields information about the kinetic-to-magnetic energy density ratio ( $\rho_{kin}/\rho_{mag}$ , Zweibel 1990).

Previous works used the CF procedure to calculate the magnetic field projected on the sky in several regions of ISM (Gonatas et al. 1990; Morris et al. 1992; Chrysostomou et al. 1994; Itoh et al. 1999; Henning et al. 2001). Nevertheless, a relatively large number of background stars are necessary in order to obtain a reasonable estimate for the strength of the magnetic field in a small area. Good statistics requires a sampling density higher enough to exceed that of the large-scale structures of the local magnetic field (Andersson & Potter 2005).

Polarimetric catalogues with several hundreds of objects in selected ISM regions and higher sampling density are now available for this type of study (Pereyra & Magalhães 2002 - Paper I, 2004) with typical value of  $\sim 1.2$  objects/arcminute<sup>2</sup> that is, at least, three orders of magnitude higher than previous works.

The *IRAS* Vela Shell (IVS) encloses a cavity that appears to have been formed by stars of the Vela OB2 association through the effects of stellar winds and supernova explosions (Sahu 1992). However, the existence of the IVS is controversial and Woermann, Gaylard, & Otrucek (2001) suggested that it is instead a density enhancement in the Gum nebula.

A section of the western side of IVS (see Figures 2 and 3 in Paper I) shows a well-defined ionization front (I-front) seen almost edge-on with several magnetic field patterns. Churchwell et al. (1996) found that the kinetic energy is one order of magnitude higher than the gravitational potential energy in this region. They concluded that the structure is not gravitationally bound and would disperse on very short timescales were it not for the ram pressure of the expanding IVS, which continually sweeps up new interstellar matter into the cloud.

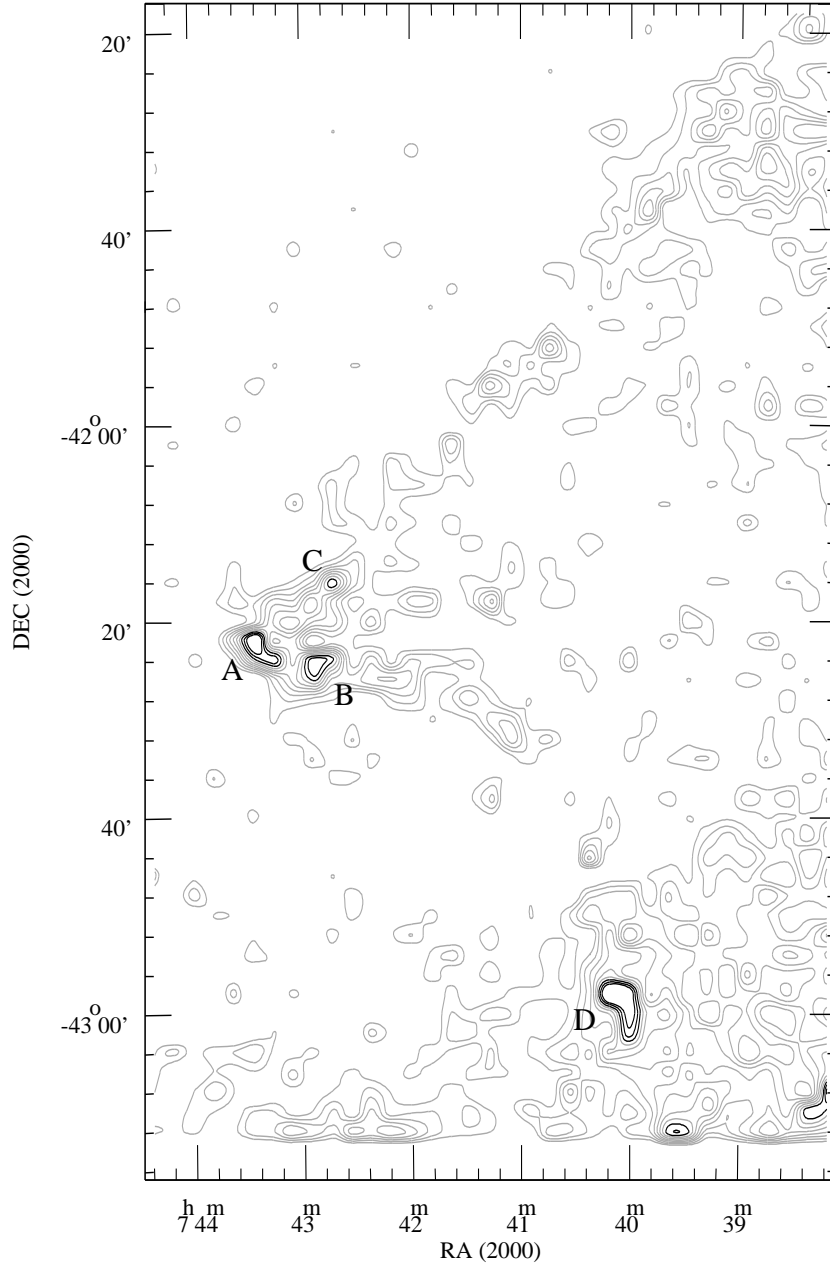


Fig. 1.— Extinction map toward the western side of *IRAS* Vela Shell. The gray contours go from 0.3 to 1.0 mag in steps of 0.1 mag. In black contours (from 1.0 to 1.2 mag) are the extinction structures (in letters) with  $A_V \geq 1$ .

In this work we explore the role of the magnetic field on the dynamics of the IVS region using a published polarimetric catalogue (Paper I), with 856 objects. In §2, we describe the technique used to construct the extinction maps. We also detect extinction structures and estimate their masses. In §3, we present a statistical analysis of the polarization catalogue. In §4, we compare the polarization along the I-front with the detected extinction structures. In §5, we apply the dispersion of polarization angle to infer the distribution of  $\rho_{kin}/\rho_{mag}$  and the strength of  $B$  along the I-front. In §6, we explore the polarizing efficiency and its implications about the amplification of the local magnetic field. In §7, we analyze the magnetic support in terms of the mass-to-magnetic flux ratio. Conclusions are drawn in §8.

Table 1. Extinction structures.

ID	RA <sub>2000</sub>	DEC <sub>2000</sub>	$A_V$	$N(\text{H}_2)$	area	$L$	mass	obs.
(1)	( h : m : s )	( ° : ' : " )	(mag)	( $10^{21}\text{cm}^{-2}$ )	( ' <sup>2</sup> )	(pc)	( $M_\odot$ )	(9)
A	07:43:26.90	-42:22:22.55	1.42	1.33	8	0.52	3.73	V12 <sup>a</sup> , A <sup>b</sup>
B	07:42:52.65	-42:24:43.90	1.16	1.09	4	0.37	1.68	B <sup>b</sup>
C	07:42:43.71	-42:16:16.90	1.05	0.99	4	0.37	1.52	–
D	07:40:05.85	-42:58:11.84	1.50	1.41	12	0.64	5.95	–

<sup>a</sup>Vilas-Boas, Myers, & Fuller (1994)

<sup>b</sup>Churchwell et al. (1996)

## 2. Visual Extinction by automatic star counts

### 2.1. The extinction map

We used our own *IRAF*<sup>1</sup> tasks to obtain maps of visual extinction of the region using an automatically star count technique. Firstly, we obtained positions of objects with stellar profiles from a *Digitized Sky Survey* image (see Figure 3 in Paper I) using the *IRAF* task *daofind*. This routine automatically detects objects over certain threshold intensity. We used a threshold of 4 times of rms sky noise on the region. Our routines count the number of stars in each cell of  $2' \times 2'$  defined on the *DSS* image and obtain the visual extinction according to Dickman (1978):

$$A_\lambda = (1/b)\log(n_0/n_1)$$

where  $n_0$  is the average number of stars in the comparison cell and  $n_1$  is the total star number obtained by the count. We obtained star count values in regions away from the filamentary structure toward the north-east around  $(\alpha, \delta)_{2000} = (07^{\text{h}}44^{\text{s}}, -41^\circ 27')$  and computed an average  $n_0 = 62$  for a box of  $20' \times 20'$ . van Rhijn (1929) tables yields the  $b$  parameter and we used  $b = 0.44$ . This value is the best compromise from averaging several lines of sight toward darks clouds (Gregorio-Hetem, Sanzovo & Lepine 1988; Andreatza & Vilas-Boas 1996). The maximum error introduced by an incorrect  $b$  value is not more of 0.3 mag for  $A_V < 1.5$  mag (see below).

We transformed the extinction obtained from digitized photographic plates ( $A_{\text{phot}}$ ) to visual extinction  $A_V$  ( $\lambda 5500\text{\AA}$ ) using the normalize extinction curve from Bless & Savage (1972). The used *DSS* image corresponds to Schmidt plates with the emulsion/filter combination IIIaJ/GC395 centered in  $4500\text{\AA}$  (Lasker et al. 1990). We obtained the necessary correction by a polynomial fit in the range  $0.4\text{--}3.4\mu\text{m}$  of the normalized extinction curve from Bless & Savage (1972) and then recalculated the extinction into the photographic band. The resulting relation was:

$$A_V = 0.79A_{\text{phot}}$$

---

<sup>1</sup>*IRAF* is distributed by the National Optical Astronomy Observatory, which is operated by the Association of Universities for Research in Astronomy, Inc., under cooperative agreement with the National Science Foundation.

We then built an extinction image of  $30 \times 60$  cells ( $= 1^\circ \times 2^\circ$ ) for the region. The error in each cell grows with the extinction value (Dickman 1978). For the cells with no star we obtained a lower limit fitting the residuals between consecutive steps of extinction and extrapolated the correction for the case  $n_1 = 0$ . This procedure resulted in assuming  $n_1 = 0.28$  for cells with no star and the corresponding lower limit of detectable maximum extinction was 4.2 mag. Nevertheless, in the regions of interest (i.e. where polarimetric data exist) the extinction is relatively low with maximum values of 1.5 mag ( $A_{V_{\max}}$ ), well below than that limit. Figure 1 shows the extinction maps obtained with this technique. The contours go from 0.3 to 1.2 mag in steps of 0.1 mag.

We must note that procedure used here to estimate the extinction is differential in origin. It means that we computed the extinction with respect to the comparison cell  $n_0$ . In order to check if a zero-point bias is present in our extinction maps, we used the reddening maps of Schlegel, Finkbeiner & Davis (1998). The average extinction in a radius of  $5'$  toward the region of the comparison cell was  $1.06 \pm 0.04^2$  mag. We consider that this level may represent the foreground extinction to the I-front. Therefore, we purposely did not correct our extinction maps by this level in order to include just the extinction associated with the I-front.

---

<sup>2</sup>see the Dust Extinction Service available at <http://irsa.ipac.caltech.edu/applications/DUST/>

Table 2. Polarization analysis.

field/ $N_{\text{cat}}$ <sup>a</sup>	trend	$\theta_{\text{gauss}}$ (deg)	$\sigma_{\theta_{\text{gauss}}}$ (deg)	$N$	$\langle P \rangle$ (%)	$\langle \sigma \rangle$ (%)	$\langle \theta \rangle$ (deg)	$\langle \sigma_{\theta} \rangle$ (deg)	$\Delta\theta$ (deg)	$(\Delta\theta)^2$ $10^{-2}$	$\langle A_V \rangle$ (mag)	$\langle n(\text{H}_2) \rangle$ ( $\text{cm}^{-3}$ )	$B$ (mG)	$\lambda$
(1)	(2)	(3)	(4)	(5)	(6)	(7)	(8)	(9)	(10)	(11)	(12)	(13)	(14)	(15)
01/14	1	...	...	14	1.105	0.005	32.9	1.2	...	...	0.34±0.24	280	...	...
02/71	1	63.7	18.1	66	0.665	0.001	61.2	1.1	18.0	9.9	0.31±0.10	255	0.008	0.27
03/68	1	69.8	15.2	43	0.703	0.005	57.9	1.8	15.1	6.9	0.23±0.12	189	0.009	0.19
04/59	1	96.5	13.2	35	1.798	0.003	104.0	0.7	13.2	5.3	0.65±0.29	535	0.016	0.28
	2	40.9	12.3	22	0.870	0.001	41.8	1.0	12.3	4.6	0.36±0.17	296	0.013	0.20
05/76	1	40.2	5.4	74	2.284	0.001	42.4	1.0	5.3	0.9	0.42±0.18	346	0.033	0.09
06/68	1	10.8	14.9	66	1.723	0.001	10.0	0.9	14.9	6.8	0.41±0.14	337	0.012	0.25
07/61	1	171.6	10.2	51	2.529	0.003	165.5	0.8	10.2	3.1	0.38±0.10	313	0.016	0.17
	2	23.5	2.9	8	2.344	0.012	23.2	0.7	2.8	0.2	0.45±0.16	370	0.064	0.05
08/68	1	32.5	8.0	65	1.701	0.003	32.9	1.0	7.9	1.9	0.32±0.08	263	0.019	0.12
09/18	1	...	...	18	0.429	0.005	95.9	1.7	...	...	0.21±0.10	173	...	...
10/78	1	...	...	78	0.057	0.001	47.3	1.1	...	...	0.18±0.09	148	...	...
11/55	1	105.3	9.5	43	0.598	0.002	109.4	1.2	9.5	2.7	0.33±0.12	271	0.016	0.15
12/62	1	15.9	14.3	29	1.623	0.001	16.0	1.0	14.3	6.2	0.44±0.34	362	0.012	0.25
	2	116.3	19.0	33	0.799	0.001	116.1	0.9	19.0	11.0	0.47±0.31	387	0.010	0.35
13/50	1	104.6	10.1	44	3.113	0.002	104.2	1.0	10.1	3.1	0.42±0.16	346	0.017	0.17
14/63	1	75.6	8.4	23	0.435	0.001	75.6	0.9	8.3	2.1	0.27±0.09	222	0.017	0.12
	2	8.1	19.3	31	0.220	0.001	9.4	1.3	19.3	11.3	0.28±0.14	230	0.007	0.27
	3	143.1	8.9	9	0.733	0.004	133.0	0.8	8.9	2.4	0.36±0.15	296	0.018	0.14
15/12	1	...	...	12	0.218	0.003	158.4	0.9	...	...	0.58±0.34	477	...	...
16/52	1	...	...	52	0.251	0.001	125.1	1.1	...	...	0.51±0.12	420	...	...

<sup>a</sup>original number of objects in each field from catalog (Paper I).|  
∞  
|



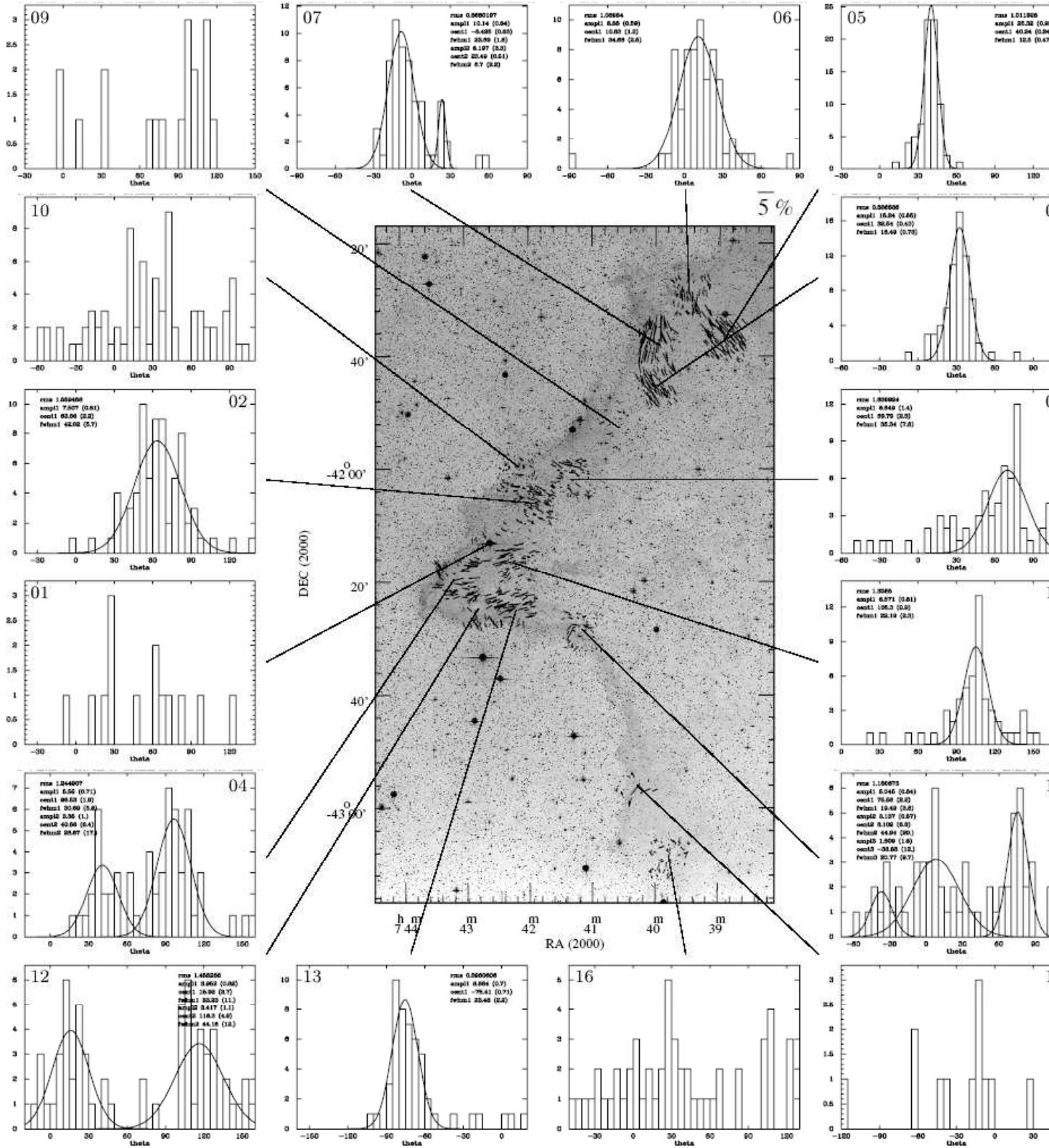


Fig. 2.— Polarization map for IVS region (see Paper I) with  $\theta$  histograms for each position analyzed (in numbers). The gaussian fits used to obtain the dispersion of polarization angles ( $\Delta\theta$ ) in each case are also shown.

## 2.2. Analysis of extinction and masses.

As noted by Churchwell et al. (1996), the IVS far-infrared dust emission follows the morphology of the I-front, implying that the radiation field of Vela OB2 and shocks induced by the expansion of the shell must heat the dust. These authors also found that the CS emission accompanies the I-front and the emission from dust.

Analyzing Figure 1 we observe that the extinction structures accompany the I-front pattern and a good correlation with the extended emission of dust exists (see Figure 2 in Paper I). Therefore, it is evident that dust, which originates the observed extinction, was shifted to the west of the I-front but accompanying its eastern pattern including the north and south curvatures observed on it. Although the extinction values are relatively small (up to  $\sim 1.5$  mag), the morphology observed on the extinction map suggests a clumpy region also invoked by Churchwell et al. (1996) using CS maps.

In order to better visualize the extinction structures, we choose regions with  $A_V \geq 1$  mag. This level is a good compromise ( $\sim \frac{2}{3} A_{V\max}$ ) to detect significant structures in our maps. Figure 1 shows these structures. We analyse some physical properties of them in Table 1. In columns (2) and (3) we show the equatorial coordinates for the positions with the highest extinction observed in each structure. In column (4) is the highest extinction value in each structure. Column (5) shows the molecular hydrogen column density estimated at the position of highest extinction in each structure using the standard gas-to-extinction ratio ( $N_{\text{H}_2}/A_V = 0.94 \times 10^{21} \text{ cm}^{-2} \text{ mag}^{-1}$ , Bohlin, Savage & Drake 1978). This ratio assumes that most of hydrogen is in molecular form and  $R_V = 3.1$ . In column (6) is the area in square arcminutes associated with each structure and estimated by adding all the cells with  $A_V \geq 1$  inside of it. Column (7) shows the dimension associated with the structure in parsecs and estimated by  $\sqrt{2(\text{area})}$ . Finally, in column (8) is a lower limit of the mass of each structure estimated using Dickman (1978):

$$M = (\alpha d)^2 (N_{\text{H}_2}/A_V) m \sum_i A_V^i,$$

where  $\alpha$  is the cell size in radians,  $d$  is the distance to the cloud in centimeters,  $(N_{\text{H}_2}/A_V)$  is the standard gas-to-extinction ratio,  $m = \mu_{\text{H}_2} m_H = 2.8 m_H$  is the mean particle mass (allowing for 10% He by number),  $\mu_{\text{H}_2}$  is the mean molecular weight with respect to the number of H molecules, and  $A_V^i$  is the visual extinction in each reseau element  $i$ .

Among the four structures (A, B, C and D) shown in Figure 1, only the A structure is coincident with the condensation named V12 in Vilas-Boas, Myers, & Fuller (1994, here-

inafter VMF) in the Vela region. In the southern dark clouds catalogue of Hartley et al. (1986), this structure has  $A_V = 6$  mag, and in VMF the extinction is  $A_V = 3.7$  mag using  $C^{18}O$  linewidths. Our extinction value ( $A_V = 1.42$  mag) is clearly the lowest. VMF also estimated the scale size, hydrogen column density and mass for V12 and obtained 0.15 pc,  $3.4 \times 10^{21} \text{cm}^{-2}$  and  $1.3 M_\odot$  (lower limit), respectively. The differences with our values in Table 1 can be traced to a lower distance used by VMF (300 pc versus 450 pc in this work) and the conversion factor of  $C^{18}O$  column density to visual extinction used by VMF ( $A_V = 6.4 \times 10^{-15} N(C^{18}O) + 3.2$  mag from Nozawa et al. 1991). In contrast, we obtained our extinction values directly from the *DSS* image.

The A and B structures in our extinction map are coincident with A and B clumps seen in the distribution study of CS column density of Churchwell et al. (1996) done in the same region. In summary, from Table 1 we estimate a range for typical masses of 1.5–6  $M_\odot$  and a mean length scale  $L \sim 0.47$  pc for the extinction structures found by us.

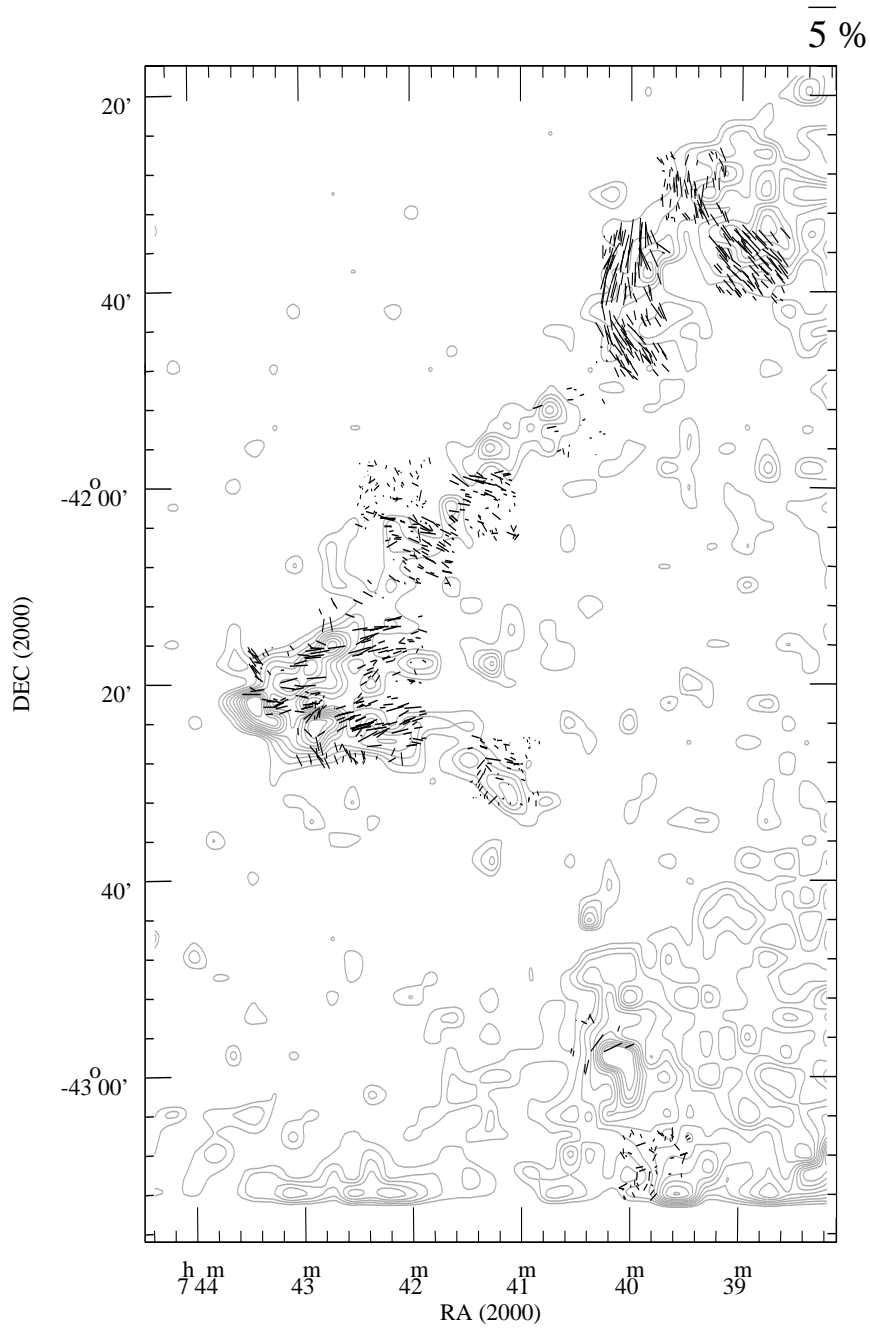


Fig. 3.— Polarization map overlaying the extinction map. The polarization scale is shown on the upper right. The contours are the same as in Fig. 1.

### 3. Polarization analysis

In order to better quantify the observed polarization pattern in each one of sixteen fields studied in Paper I, we present a statistical analysis in Table 2. Each field is given in column (1), together with the catalog stars within the field ( $N_{\text{cat}}$ ). We construct polarization angle histograms (see Figure 2) for each field and used gaussian fits to obtain the representative polarization angle  $\theta_{\text{gauss}}$  and its dispersion  $\sigma_{\theta_{\text{gauss}}}$ , indicated in columns (3) and (4). In general, one trend prevails in each field but, in some fields, two or three trends appear, and this is indicated in column (2). In a few of fields, the star sample was poor, the fit was not possible and there is no evident trend. It is interesting to note that none one of the polarization trends is parallel to the mean direction of the Galactic Plane ( $\theta \sim 151^\circ$ ) toward this line of sight ( $l = 256^\circ$ ,  $b = -9.2^\circ$ ). This suggests that the polarization data is indeed sampling the local magnetic field associated with the IVS region.

To improve on the precision of the mean polarization values for each trend, we included a filter in each field. We select those objects with polarization angle between ( $\theta_{\text{gauss}} - 2 \times \sigma_{\theta_{\text{gauss}}}$ ,  $\theta_{\text{gauss}} + 2 \times \sigma_{\theta_{\text{gauss}}}$ ). The number ( $N$ ) of stars with  $P/\sigma_P \geq 10$  in each filtered subsample is given in column (5). We then estimated the mean Stokes parameters,  $\langle Q \rangle$  and  $\langle U \rangle$ , for each subsample, from the individuals values for each star ( $q_i$ ,  $u_i$ ) weighted by the error ( $\sigma_i$ ) according to:

$$\begin{aligned}\langle Q \rangle &= \sum (q_i / \sigma_i^2) / \sum \sigma_i^{-2} \\ \langle U \rangle &= \sum (u_i / \sigma_i^2) / \sum \sigma_i^{-2}.\end{aligned}$$

The estimated mean polarization value  $\langle P \rangle$ , its associated error  $\langle \sigma \rangle$  and its mean polarization position angle  $\langle \theta \rangle$  are then given by:

$$\begin{aligned}\langle P \rangle &= \sqrt{\langle Q \rangle^2 + \langle U \rangle^2} \\ \langle \sigma \rangle &= (1 / \sum \sigma_i^{-2})^{0.5} \\ \langle \theta \rangle &= 0.5 \tan^{-1}(\langle U \rangle / \langle Q \rangle).\end{aligned}$$

These are presented in columns (6), (7) and (8). We show the mean error of the polarization angle in column (9). This was estimated from  $\langle \sigma_\theta \rangle = \sum \sigma_{\theta_i} / N$  where  $\sigma_{\theta_i} = 28.65 \sigma_{p_i} / p_i$

is the individual error of the polarization position angle (Serkowski 1974) for an star with polarization ( $p_i \pm \sigma_{p_i}$ ). Column (10) shows the dispersion of polarization angles corrected in quadrature by its mean error ( $\Delta\theta = \sqrt{\sigma_{gauss}^2 - \langle\sigma_\theta\rangle^2}$ ); column (11) shows the squared of this dispersion (in radians).

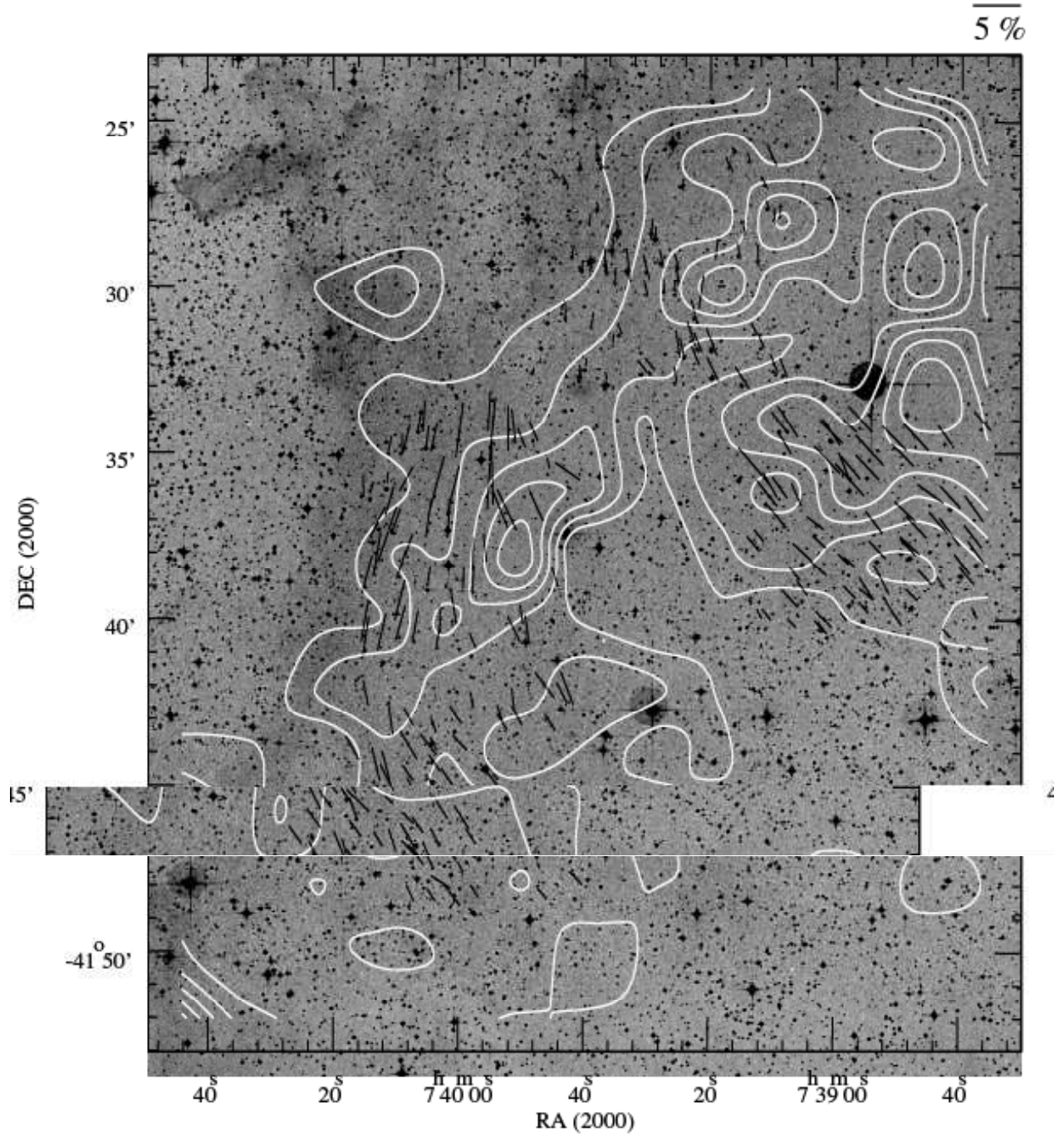


Fig. 4.— Polarization map overlapping the extinction map for fields 05, 06, 07 and 08. The polarization scale is shown up to the right. The contours are the same as in Fig. 1.

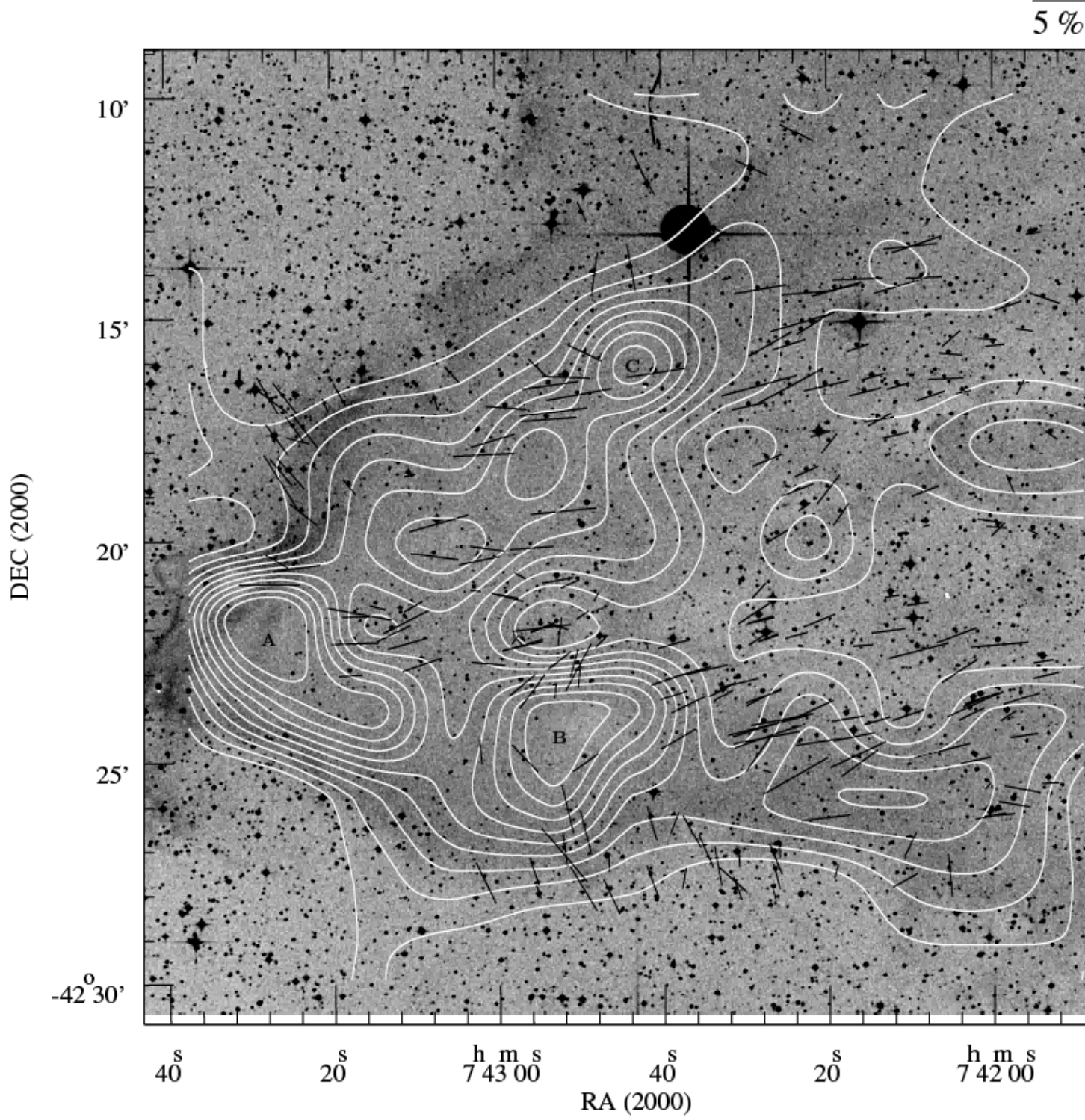


Fig. 5.— Polarization map overlapping the extinction map for fields 01, 04, 11, 12 and 13. The polarization scale is shown up to the right. The contours are the same as in Fig. 1. The condensations A, B and C are also indicated.



#### 4. Polarization and extinction

To help our analysis of correlations between polarization and extinction, we estimated the average extinction for objects in each one of the polarization trends (column (12) of Table 2). The position of each star in the polarimetric catalogue is well determined with a typical precision of less than  $1''$ . We then identified its position in the extinction maps and attributed the value of the extinction cell where the star was located. This procedure may underestimate the extinction value assigned to a star because the resolution of  $2' \times 2'$  of the extinction maps may not resolve variations of extinction within one extinction cell.

Figure 3 plots the extinction map of Figure 1 along with the polarization map (Figure 5 in Paper I) of the region. The polarization vectors, which are from stars with  $P/\sigma_P > 10$  in the catalog, are concentrated in regions with significant extinction along the I-front. The extinction is low ( $A_V \leq 1.5$  mag) but is enough to produce the observed polarization. The range of extinction sampled by our polarization data is similar to the extinction found in the outer layers of darks clouds and in the diffuse ISM ( $A_V < 3$  mag, Vrba & Rydgren 1985; Kenyon, Dobrzycka & Hartmann 1994) and below the threshold extinction of the transition from bare to H<sub>2</sub>O-mantled grains ( $A_V \sim 3.3$  mag, Gerakines, Whittet & Lazarian 1995; Whittet et al. 2001).

In order to quantify the interval of extinction sampled by our catalogue, we analysed two subregions (shown in Figures 4 and 5) with well defined polarization patterns.

Figure 4 shows the four fields (05, 06, 07 and 08) at the top of northern ridge (see Figure 2) around  $(\alpha, \delta)_{2000} = (07^{\text{h}}39^{\text{m}}5, -41^{\circ}37')$ . This region presents an observed polarization higher than average and a very smooth overall pattern as noted in Paper I. The range of mean polarization goes from 1.7% to 2.5% and the mean extinction from 0.32 to 0.45 mag. It is interesting to note that the fields 06 and 07 (trend 1), closer to I-front wall and aligned with it, present a dispersion of polarization angle ( $\Delta\theta$ ) at least twice than ones of the fields 05 and 08. It reinforces the suggestion of a magnetic field enhancement in the compressed postshock gas as indicated in Paper I.

The region shown in Figure 5 (fields 01, 04, 11, 12 and 13; see Figure 2) presents a very complex polarization pattern. This complexity seems associated with the A, B and C extinction structures. This region has a range of mean polarization of 0.6%–3.1% with the highest value in field 13. The mean extinction goes from 0.33 to 0.47 mag. As we will see in §6, the larger range of polarization values is a indication of significant variations in the polarization efficiency in small angular scales in this subregion.

In some fields, our detection of trends through  $\theta$  gaussian fits fails in cases where a good polarimetric sample seems to be present. This is evident in fields 09, 10 and 16 (see

Figure 2). Nevertheless, a non-detection of a polarization trend seems correlated with low extinction regions as can be verified by the mean extinction of fields 09 and 10 that are 0.21 mag and 0.19 mag, respectively. However, field 16 has a high mean extinction (0.51 mag) but this value may be affected by the contrast gradient present at the border of the *DDS* image used.

## 5. Magnetic fields

As we noted in §1, CF gives an estimate of the magnetic field component ( $B$ ) on the plane of the sky:

$$B = (4\pi\rho)^{1/2}\nu/\Delta\theta \quad (1)$$

where,  $B$  is in gauss (G),  $\rho$  is the density ( $\text{g cm}^{-3}$ ),  $\nu$  is the turbulent motion velocity ( $\text{cm s}^{-1}$ ) and  $\Delta\theta$  is in radians. In terms of energy densities, the ratio of the kinetic energy density ( $\rho_{kin} \propto \rho\nu^2$ ) to magnetic energy density ( $\rho_{mag} \propto B^2$ ) is the mean square fluctuation of  $B$  (Zweibel 1990), so

$$(\rho_{kin}/\rho_{mag}) \propto (\Delta\theta)^2.$$

Therefore,  $\rho_{kin}/\rho_{mag}$  and/or  $B$  can be obtained from  $\Delta\theta$  (column (10) in Table 2). In some fields (01, 09, 10, 15, and 16), it was not possible to obtain information of  $\Delta\theta$  because of a poor polarimetric sample or the polarimetric pattern is random. In the remaining fields, we estimated  $(\Delta\theta)^2$  for each trend (column (11) of Table 2). We can note that  $(\Delta\theta)^2$  shows a range of  $(0.2-11.3)\times 10^{-2}$ . This can be interpreted as variations of (at least) one order of magnitude in  $\rho_{kin}/\rho_{mag}$  along the region. Nevertheless, this large variation range observed in  $(\Delta\theta)^2$  is consistent with the fact that some regions present random position angles. Extreme cases would be fields 09, 10 and 16, where the impossibility of estimating  $\Delta\theta$  may be interpreted as the kinetic energy density prevailing over the magnetic energy density.

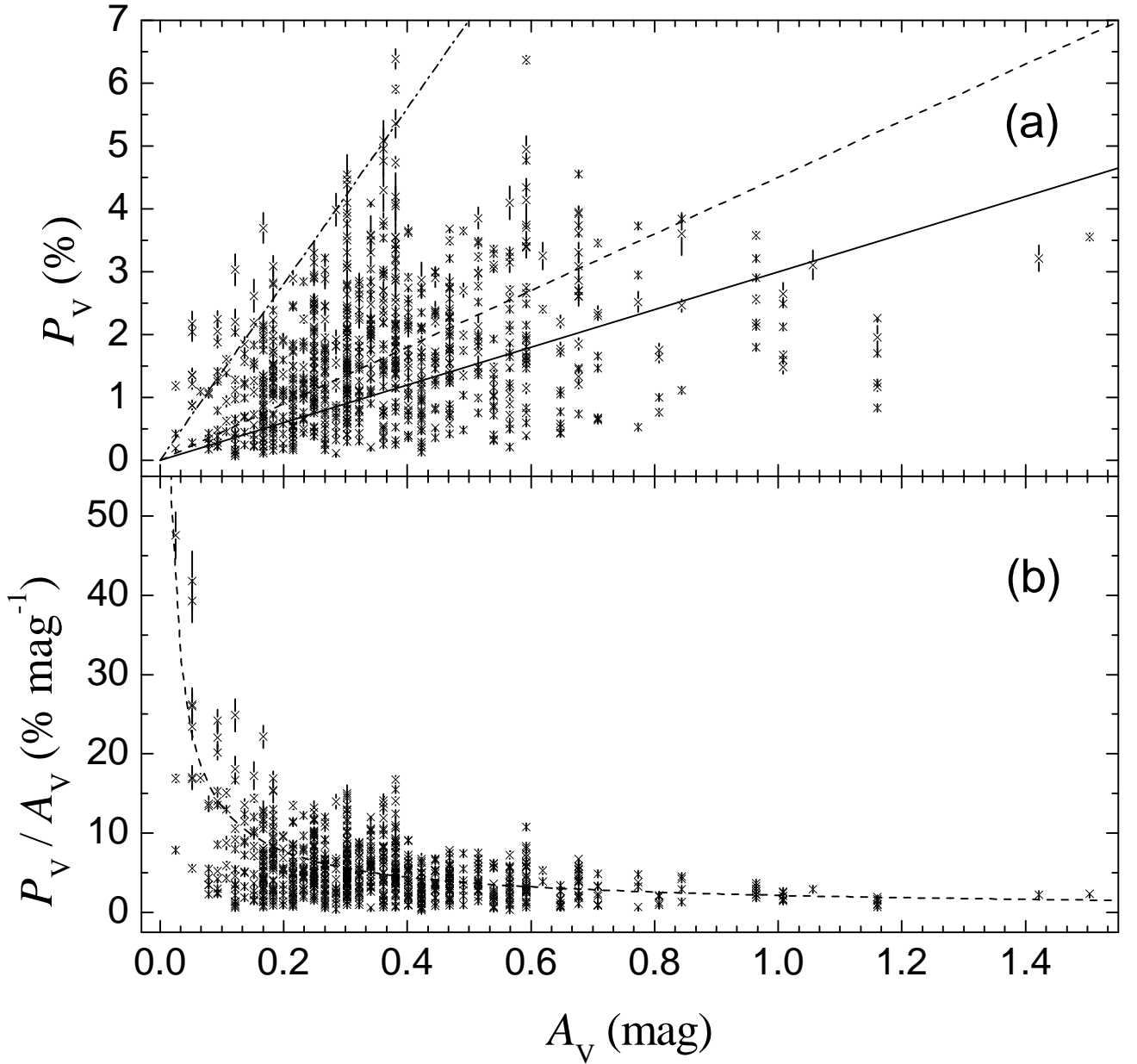


Fig. 6.— (a) Polarization versus visual extinction. The solid line represents the higher limit for ISM polarization ( $P_{max} = 3A_V$ ; Serkowski, Mathewson & Ford 1975). The dashed line represents the higher limit towards Cha I ( $P_{max} = 4.5A_V$ ; Whittet et al. 1994). The dot-dashed line is the upper limit ( $P = 14A_V$ ) for dust grains consisting of completely aligned infinite dielectric cylinders (Whittet 1992) that covers 96.3% of the sample. (b) Polarizing efficiency versus extinction. The dashed line represents a least-squares power-law fit to our sample ( $P_V/A_V = 2.54 \pm 0.08 A_V^{-0.61 \pm 0.04}$  % mag $^{-1}$ ).

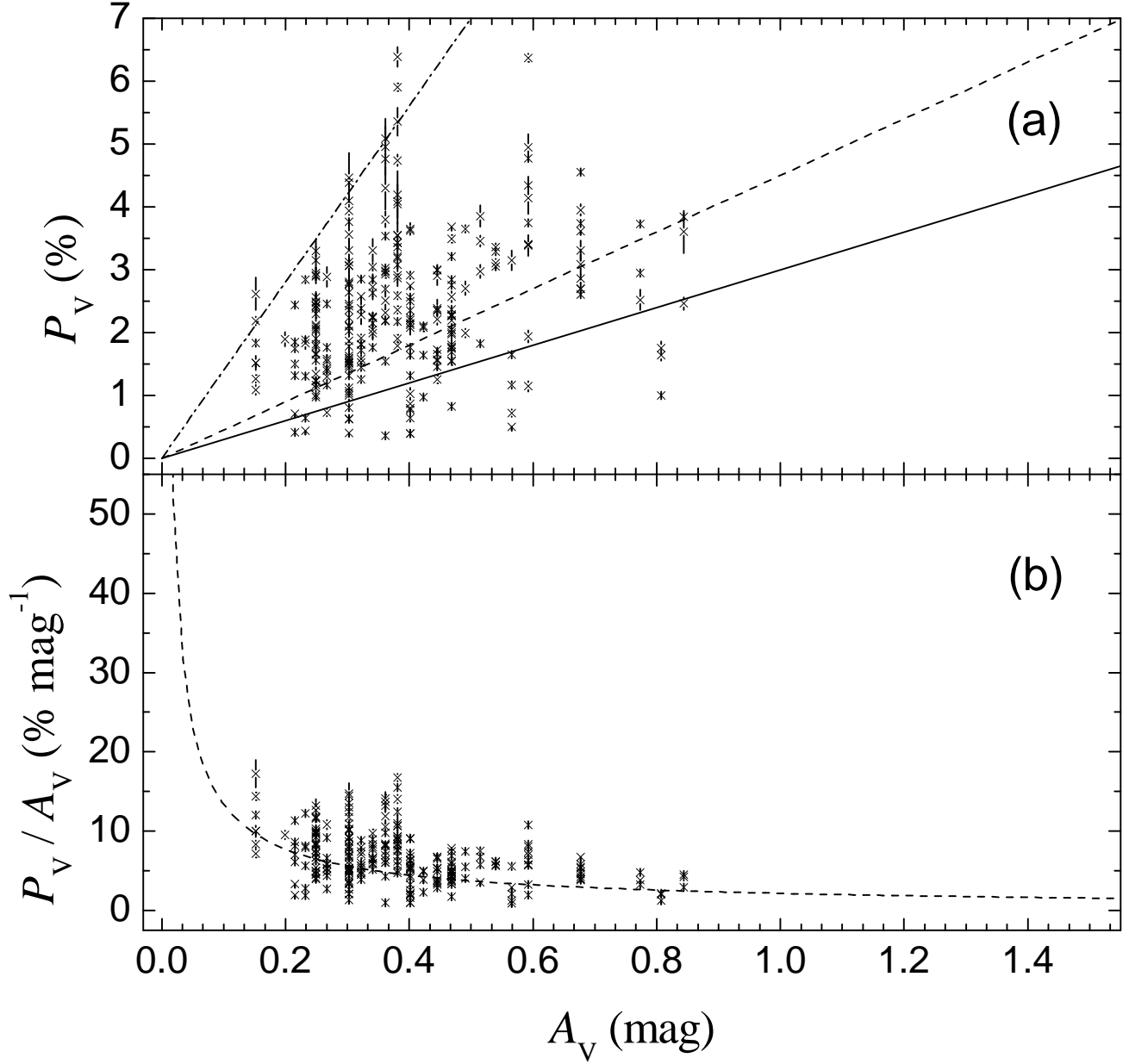


Fig. 7.— (a) Polarization versus visual extinction for fields in Figure 4. The solid, dashed and dot-dashed lines as in Figure 6. (b) Polarizing efficiency versus extinction. The dashed line represents a least-squares power-law fit to this sub-sample ( $P_V/A_V = 3.50 \pm 0.25 A_V^{-0.60 \pm 0.07} \% \text{ mag}^{-1}$ ).

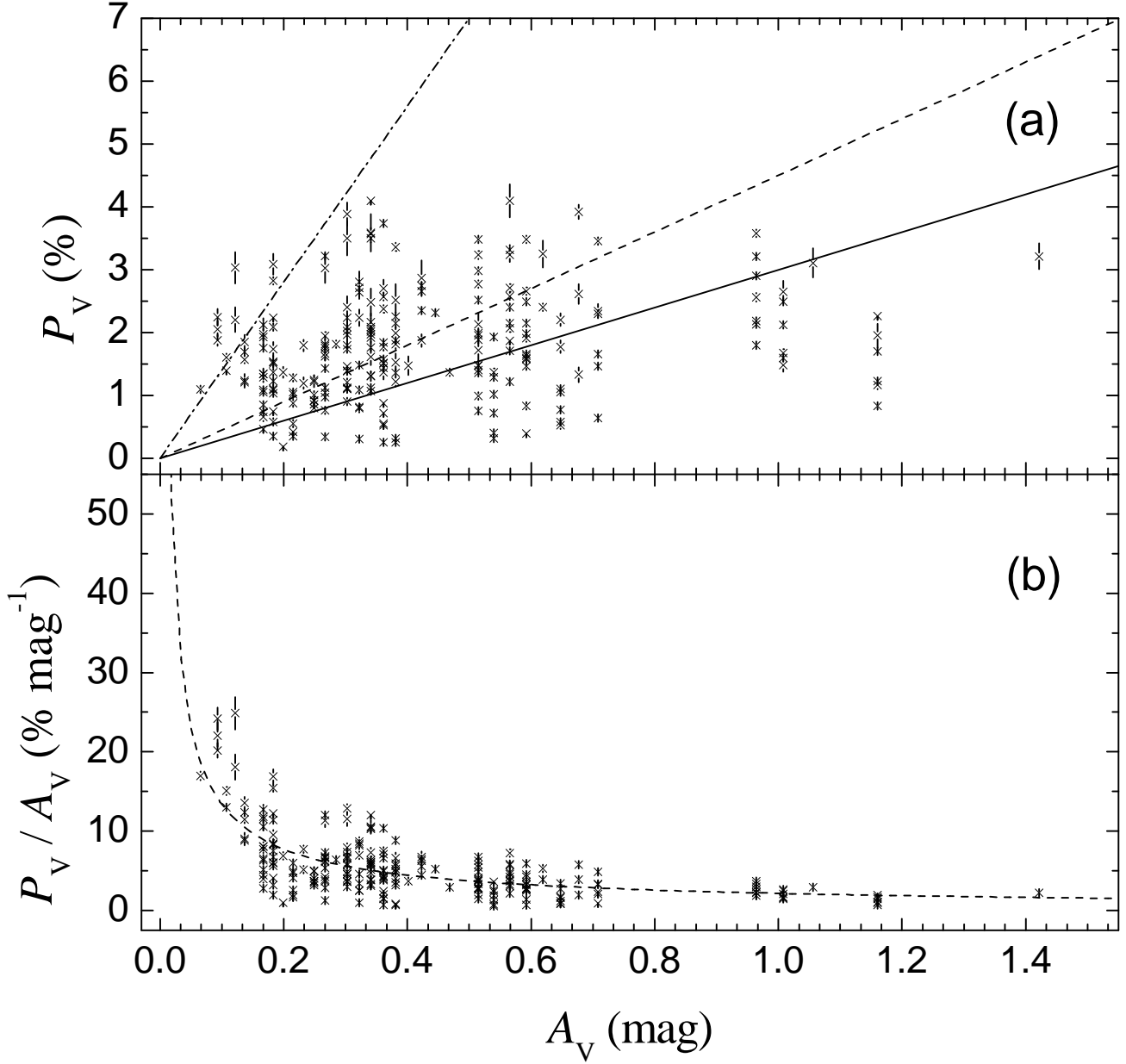


Fig. 8.— (a) Polarization versus visual extinction for fields in Figure 5. The solid, dashed and dot-dashed lines as in Figure 6. (b) Polarizing efficiency versus extinction. The dashed line represents a least-squares power-law fit to this sub-sample ( $P_V/A_V = 2.16 \pm 0.14 A_V^{-0.79 \pm 0.07} \% \text{ mag}^{-1}$ ).

In order to calculate the strength of the magnetic field, we assume that the turbulent velocity ( $\nu$ ) is represented by the dispersion velocity of a Gaussian distribution ( $\Delta V^2 = 8\ln 2 \nu^2$ ) where  $\Delta V$  is obtained from the mean FWHM of an appropriate molecular line. This dispersion may represent the gas, of density  $\rho$ , in which the polarization arises. The CS emission in this region yields  $\Delta V_{\text{CS}} = 1.4 \text{ km s}^{-1}$  (Churchwell et al. 1996). As noted by these authors, the density,  $\rho = mn(\text{H}_2)$ , needed for CS excitation requires a particle density  $n(\text{H}_2) \sim 10^4 \text{ cm}^{-3}$ . As the CS emission samples the higher density cores, its density may represent a higher limit for the outer layers of dust clouds which our polarization measurements sample. Vilas-Boas, Myers, & Fuller (2000) analysed CO emission in the Vela region and found mean dispersions of  $\Delta V_{13\text{CO}} = 0.7 \pm 0.2 \text{ km s}^{-1}$  and  $\Delta V_{\text{C}18\text{O}} = 0.6 \pm 0.2 \text{ km s}^{-1}$ . As the CO emission probably samples the envelope regions of molecular clouds, its dispersion may better represent the turbulent motions. Therefore, we believe that a dispersion of  $\Delta V = 1.0 \text{ km s}^{-1}$  is a good compromise to consider as input parameter in our computation.

We used the average extinction (column (12) of Table 2) to infer the mean particle density  $\langle n(\text{H}_2) \rangle$  in each polarization trend. We take,

$$\langle n(\text{H}_2) \rangle = \langle A_V \rangle (N_{\text{H}_2} / A_V) \frac{1}{l},$$

where  $l$  is the typical size (in parsecs) of an extinction cell assuming a distance of 450 pc. The computed values are indicated in column (13) of Table 2. The overall average density from the trends is  $312 \pm 97 \text{ cm}^{-3}$ . This value is consistent with our sampling the low density regions, as discussed above, and will be used in the following.

Therefore, with the above parameters and using eq. 1, the magnetic field expression becomes:

$$B(\text{G}) = 2.88 \times 10^{-6} \left( \frac{n(\text{H}_2)}{312 \text{ cm}^{-3}} \right)^{1/2} \left( \frac{\Delta V}{1.0 \text{ km s}^{-1}} \right) / \Delta\theta.$$

In this way, we estimated  $B$  (column (14) of Table 2) for each field and for each trend with a well defined dispersion of polarization angle ( $\Delta\theta$ ). Ostriker et al. (2001) noted that  $\Delta\theta < 25^\circ$  yields a good estimate of the plane-of-sky magnetic field strength if a multiplying factor of  $\sim 0.5$  is applied to CF formula. As we can note in Table 2, all the  $\Delta\theta$  values are lower than this limit and the above expression also include this correction. As usual, use

of the CF formula for estimating  $B$  carries an uncertainty from all discussed here. Apart from the above mentioned multiplying factor, the uncertainties in  $n(\text{H}_2)$ ,  $\Delta V$  and  $\Delta\theta$  imply a typical uncertainty of at least 50% in  $B$ .

The average strength of the magnetic field along the I-front is  $[0.018 \pm 0.013]$  mG and the full range of variation is  $\sim$ one order of magnitude (0.007–0.064 mG). As Zweibel (1990) pointed out, if the line of sight samples  $\mathcal{N}$  different regions with different magnetic orientations,  $B$  would tend to be overestimated by  $\sqrt{\mathcal{N}}$ . This averaging effect may be important, for example, in the region of complex polarization pattern showed in Figure 5 where *clumpy* structures are present.

Finally, Churchwell et al. (1996) concluded that the potential energy of this region is just  $\sim 0.05$  of the total kinetic energy (thermal plus turbulent) and the expanding shell pressure avoids the dissipation of the region. From the estimates of  $B$  along with the observed fact that, in general, the magnetic pressure dominates over the turbulent pressure in several parts of the shell, we conclude that the magnetic component also contributes in an important way to the dynamical balance of this region.

## 6. Polarizing efficiency

We combined our polarization data with the extinction maps obtained by star counts to analyze the polarizing efficiency of the dust in the region. Figure 6a plots the visual polarization percentage versus the visual extinction for the 856 objects in the catalogue.

As we noted above, the extinction range in our sample extends up to  $\sim 1.5$  mag and the maximum polarization is  $\sim 6\%$ . The solid line in Figure 6a represents the upper limit for optimum polarization efficiency in diffuse ISM ( $P_{max} = 3A_V$ ; Serkowski, Mathewson & Ford 1975) and just 30.2% of the sample is under this limit. Whittet et al. (1994) found a higher upper limit for optimum polarization ( $P_{max} = 4.5A_V$ ) toward some lines of sight in the Cha I dark cloud. They concluded that a high degree of alignment is present with the magnetic field lines essentially perpendicular to our line of sight. If we consider this upper limit (dashed line in Figure 6a) the percentage of our sample under this limit rises to 49.8%.

It seems to be clear that part of the dust that produces the observed alignment in this region has different properties than diffuse ISM dust and it is especially true for low extinction ( $A_V < 0.8$  mag) regions. On the other hand, the higher polarization efficiency for low extinction can be an indicator that an optimum alignment is present in some regions of I-front maybe favored by a privileged geometric view (i.e. parallel to plane of the sky) of the magnetic field with respect to the wall seen edge-on. This fact can be quantified by

the theoretical upper limit ( $P_V/A_V \lesssim 14$ ) for dust grains consisting of completely aligned infinite dielectric cylinders (Whittet 1992) that covers 96.3% of the sample (dot-dashed line in Figure 6a).

Nevertheless, and as mentioned in §4, the possibility of our  $2' \times 2'$  extinction cell will be underestimating the extinction can not be discarded. If this is the case, higher extinction values can be masked by the observed clumpy structures and an optimum alignment better than different dust properties is more plausible to explain the correlations found.



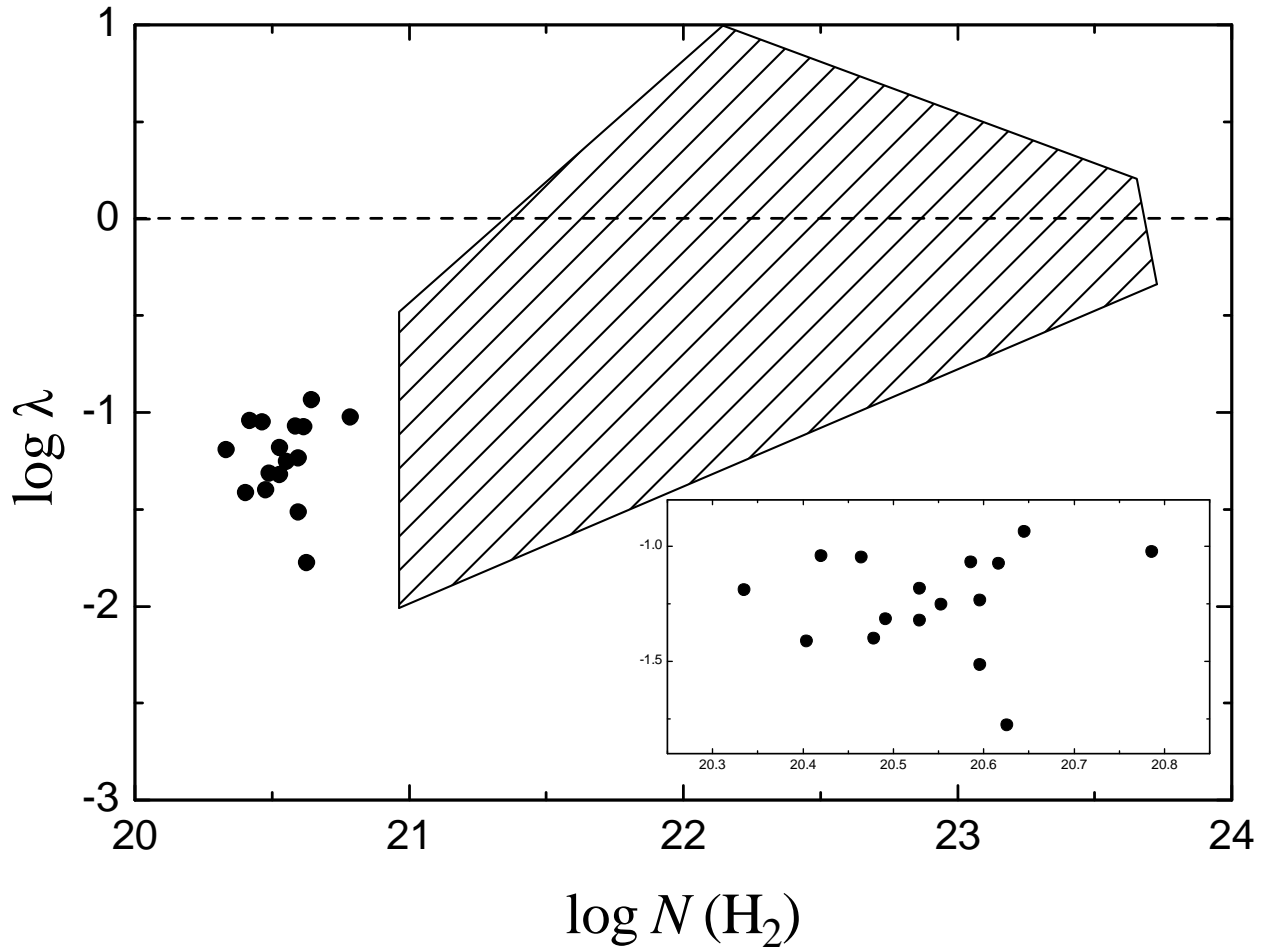


Fig. 9.— Observed mass-to-magnetic flux ratio in units of the critical value (corrected by bias projection) versus molecular column density. In black dots are the  $\lambda$ s evaluated in each polarization trend (with  $B$  estimated) from Table 2. The IVS region is dominated by the subcritical regime ( $\lambda < 1$ ). The dashed region represents all the  $\lambda$ s available for molecular clouds (Chutcher 2004). The box inside the figure is a zoom to show more detail.

In Figure 6b, we plot the polarizing efficiency versus the extinction and it is very clear as regions with low extinction are more efficient to polarize the light of background stars than high extinction regions. This fact already has been observed previously in darks clouds (Vrba, Strom, & Strom 1976; Vrba, Coyne, & Tapia 1981; Vrba, Marraco & Strom 1992; Vrba, Coyne, & Tapia 1993; McGregor et al. 1994; Whittet et al. 1994; Gerakines, Whittet & Lazarian 1995; Goodman et al. 1995). However, in I-fronts of shells in expansion, as this study, previous evidence does not exist in literature.

The dashed line in Figure 6b shows a least-squares power-law fit to our sample ( $P_V/A_V = 2.54 \pm 0.08 A_V^{-0.61 \pm 0.04} \% \text{ mag}^{-1}$ ). The dependence of the polarizing efficiency with the extinction found by us is very close to the models of Jones (1989,  $P/A \propto A^{-0.5}$ ) that assumes a magnetic field with random and uniform components. Our fit also compares very well with Gerakines, Whittet & Lazarian (1995,  $P/A \propto A^{-0.56 \pm 0.17}$ ) for observed data in Taurus dark cloud.

The ratio  $P/A$  may be written as  $P/A \propto A^{2k-1}$  (Gerakines, Whittet & Lazarian 1995), where  $k$  represents the amplification of the magnetic field with a gas density (Mouschovias 1978,  $B \propto n^k$ ). Our fit yields  $k = 0.195$ . This value is below the observed lower limit ( $k = 0.33$ ) of Mouschovias (1978) and the models of magnetic fields in turbulent molecular clouds (Ostriker et al. 2001). As pointed out by Gerakines, Whittet & Lazarian (1995) this discrepancy could be result of ignoring effects of small-scales inhomogenties in the magnetic field and of the coupling of gas and dust temperatures in regions of high density in the assumed polarizing efficiency ( $P/A \propto B^2/n$  from Vrba, Coyne, & Tapia 1981, 1993). Finally, the coefficient of our fit (2.54) is close to  $P/A = 3$  (from Serkowski, Mathewson & Ford 1975) and this suggests that the higher extinction regions ( $0.8 < A_V < 1.5$ ) of our sample are more *normal* and comparable to diffuse ISM.

As comparison, we made the same as analysis for the two subsamples shown in Figures 4 and 5. The results are shown in Figures 7 and 8, respectively. As we can note, the region sampled in Figure 4 corresponds to low extinctions, below  $\sim 0.8$  mag. We find a high polarizing efficiency and this subsample seems to be representative of the overall trend observed in the full sample (Figure 6). Note that the exponents of the fits for this subsample and the full sample are essentially the same. On the other hand, the very complex polarization pattern shown in the region indicated in Figure 5 has a higher extinction range (up to  $\sim 1.5$  mag, Figure 8) and the polarizing efficiency is lower if compared with the previous region.

## 7. Mass-to-flux ratio

Cardelli & Savage (1988) noted that *IRAS* point sources are coincident with the densest portion of this region. They speculated that shocks might have triggered local collapse and possibly star formation. However, they associated the clumpy structure seen in this region with clumps of warm dust with peak emission in 60 $\mu$ m band and star formation was ruled out.

The importance of magnetic fields in the evolution of interstellar clouds and star formation can be tested if the mass-to-magnetic flux ratio can be quantified ( $M/\Phi$ ). We can evaluate this issue using the  $\lambda$  parameter (Chrutcher et al. 2004, and references therein) defined as:

$$\lambda \equiv \frac{(M/\Phi)_{actual}}{(M/\Phi)_{crit}} = 7.6 \times 10^{-21} \frac{N(\text{H}_2)}{B}, \quad (2)$$

where  $(M/\Phi)_{crit}$  is the critical value for the mass that can be supported by a magnetic flux,  $N(\text{H}_2)$  is in  $\text{cm}^{-2}$  and  $B$  is in  $\mu\text{G}$ . In the subcritical regime ( $\lambda < 1$ ), magnetic support prevents the collapse and the star formation and probably this is the case in the IVS region.

We evaluated the  $\lambda$  parameter (using eq. 2) for each polarization trend where  $B$  has been estimated. The results are indicated in the last column of Table 2. We obtained  $N(\text{H}_2)$  from the mean extinction  $\langle A_V \rangle$  for each trend (column (12) in Table 2) and using the standard gas-to-extinction ratio (as in §2.2). As  $\langle A_V \rangle$  and  $B$  are estimated in exactly the same area, this guarantees a proper determination of  $\lambda$ . Clearly, all the regions with an alignment trend are in the subcritical regime ( $\lambda < 1$ ) between 0.05 and 0.35. If we applied the 1/3 correction factor to take in count the projection bias (Chrutcher et al. 2004), the subcritical regime is even sharper. This is evident in Figure 9 that shows the distribution of  $\lambda$  (corrected by projection bias) as a function of the molecular column density.

It seems clear that magnetic support is important in the IVS region and the data are consistent with the prediction of ambipolar diffusion models with cloud envelopes being initially subcritical. This is also consistent with non-star formation in this region as speculated by Cardelli & Savage (1988).

It is interesting to note that the two points with the largest column densities and largest  $\lambda$ s (Figure 9) correspond to polarization trends associated with the high extinction structures A and B (see §2.2). Chrutcher (2004) analyzed all the  $\lambda$ s available for molecular clouds (dashed region in Figure 9) and noted a slight indication that for large column densities,  $\lambda$  may be supercritical, and for small column densities, subcritical. Although that our data in

Figure 9 samples just a interval of lower  $N(\text{H}_2)$  values ( $\sim 10^{20} \text{ cm}^{-2}$ ), evidence of  $\lambda$  rises with  $N(\text{H}_2)$  can not be discarded.

## 8. Conclusions

Our conclusions can be summarized as follows:

1. Extinction maps obtained using automatic star counts toward the western side of *IRAS* Vela Shell yield evidence of clumpy structures with typical lower limits of masses between 1.5 and 6  $M_\odot$  and a length scale  $L \sim 0.47$  pc (assumed a distance of 450 pc).

2. We estimated the strength of the local magnetic field on the plane of the sky using the dispersion of polarization angles and educated estimates for other cloud properties. The mean value computed along the I-front was  $[0.018 \pm 0.013]$  mG and the full range of variation was (0.007–0.064) mG. In terms of energy densities, the magnetic pressure generally dominates over the turbulent motions along the I-front. In a few cases, the polarization angle appears to change randomly, suggesting that the kinetic energy can dominate.

3. We also investigated the polarizing efficiency combining the polarization data with the extinction maps. We found high polarizing efficiency in low extinction regions. It can be explained by different properties of dust as compared with the general ISM dust. Another more plausible possibility to explain this high polarizing efficiency is an optimum mechanism of dust alignment maybe favored by the magnetic field lines are nearly parallel to the plane of the sky and perpendicular to the I-front.

4. Using the strength of magnetic field and the extinction estimated in each polarization trend was possible to evaluate the mass-to-magnetic flux ratio along the IVS region. The range of the  $\lambda$  parameter we found (0.05–0.35) confirms that the magnetic support is dominant along this I-front and a subcritical regime prevails. The  $\lambda-N(\text{H}_2)$  relation we find joins smoothly the overall relation previously obtained for higher density regions. This provides general support for the evolution of initially subcritical clouds to an eventual supercritical stage.

The authors wish to thank the anonymous referee for his/her careful reading and suggestions that helped to improve the paper. AP is thankful to CAPES and FAPESP (grant 02/12880-0) for financial support. AMM acknowledges support from FAPESP and CNPq. Polarimetry at IAG-USP is supported by a FAPESP grant 01/12589-1.

## REFERENCES

- Andersson, B-G., & Potter, S. B. 2005, MNRAS, 356, 1088
- Andreazza, C. M., & Vilas-Boas, J. W. S. 1996, A&AS, 116, 21
- Bless, R. C., Savage, B. D. 1972, ApJ, 171, 293
- Bohlin, R. C., Savage, B. D., & Drake, J. F. 1978, ApJ, 224, 132
- Cardelli, J. A., & Savage, B. D. 1988, ApJ, 325, 864
- Chandrasekhar, S., & Fermi, E. 1953, ApJ, 118, 113
- Churchwell, E., Winnberg, A., Cardelli, J., Cooper, G., & Suntzeff, N. B. 1996, ApJ, 469, 209
- Chrysostomou, A., Hough, J. H., Burton M. G., & Tamura, M. 1994, MNRAS, 268, 325
- Crutcher, R. M. 2004, Ap&SS, 292, 225
- Crutcher, R. M., Nutter, D. J., Ward-Thompson, D., & Kirk, J. M. 2004, ApJ, 600, 279
- Dickman, R. L. 1978, AJ, 83, 363
- Draine, B. T., & McKee, C. F. 1993, ARA&A, 31, 373
- Gerakines, P. A., Whittet, D. C. B., & Lazarian, A. 1995, ApJ, 455, L171
- Goodman, A. A., Jones, T. J., Lada, E. A., & Myers, P. C. 1995, ApJ, 448, 748
- Gonatas, D. P., Engargiola, G. A., Hildebrand, R. H., Platt, S. R., Wu, X. D., Davidson, J. A., Novak, G., Aitken, D. K., & Smith, C. 1990, ApJ, 357, 132
- Gregorio-Hetem, J. C., Sanzovo, G. C., & Lepine, J. R. D. 1988, A&AS, 76, 347
- Hartley, M., Manchester, R. N., Smith, R. M., Tritton, S. B., & Goss, W. M. 1986, A&AS, 63, 27
- Hartquist, T. W., Pilipp, W., & Havnes, O. 1997, Ap&SS, 246, 243
- Henning, Th., Wolf, S., Launhardt, R., & Waters, R. 2001, ApJ, 561, 871
- Itoh, Y., Chrysostomou, A., Burton, M., Hough, J. H., & Tamura, M. 1999, MNRAS, 304, 406.

- Jones, T. J. 1989, *ApJ*, 346, 728
- Kenyon, S. J., Dobrzycka, D., & Hartmann, L. 1994, *AJ*, 108, 1872
- Lasker, B. M., Sturch, C. R., McLean, B. J., Russell, J. L., Jenkner, H., & Shara, M. M. 1990, *AJ*, 99, 2019
- McGregor, P. J., Harrison, T. E., Hough, J. H., & Bailey, J. A. 1994, *MNRAS*, 267, 755
- Morris, A., Davidson, J. A., Werner, M., Dotson, J., Figer, D. F., Hildebrand, R., Novak, G., & Platt, S. 1992, *ApJ*, 399, L63
- Mouschovias, T. Ch. 1978, in *Protostars and Planets*, ed. T. Gehrels (Tucson: Univ. Arizona Press), p 209
- Nozawa, S., Mizuno, A., Teshima, Y., Ogawa, H., & Fukui, Y. 1991, *ApJS*, 77, 647
- Ostriker, E. C., Stone, J. M., & Gammie, C. F. 2001, *ApJ*, 546, 980
- Pereyra, A., & Magalhães, A. M. 2002, *ApJS*, 141, 469 (Paper I)
- Pereyra, A., & Magalhães, A. M. 2004, *ApJ*, 603, 584
- Pilipp, W., Hartquist, T. W., & Havnes, O. 1990, *MNRAS*, 243, 685
- Pilipp, W., & Hartquist, T. W. 1994, *MNRAS*, 267, 801
- Redman, M. P., Williams, R. J. R., Dyson, J. E., Hartquist, T. W., & Fernandez, B. R. 1998, *A&AS*, 331, 1099
- Sahu, M. S. 1992, Ph. D. thesis, Rijksuniversiteit Groningen
- Schlegel D. J., Finkbeiner, D. P., & Davis, M. 1998, *ApJ*, 500, 525
- Serkowski, K. 1974, in Carleton N., ed., *Methods of Experimental Physics*, 12, Part A. Academic Press, New York, p. 361
- Serkowski, K, Mathewson, D. S., & Ford, V. L. 1975, *ApJ*, 196, 261
- Spitzer, L. 1978, *Physical Processes in the Interstellar Medium* (New York: Wiley), 221
- Troland, T. H., & Heiles, C. H. 1982, *ApJ*, 260, L19
- van Rhijn, P. J. 1929, *Publ. Astron. Lab. Groningen*, No. 43
- Vilas-Boas, J. W. S., Myers, P. C., & Fuller, G. A. 1994, *ApJ*, 433, 96

- Vilas-Boas, J. W. S., Myers, P. C., & Fuller, G. A. 2000, *ApJ*, 532, 1038
- Vrba, F. J., Strom, S. E., & Strom, K. M. 1976, *AJ*, 81, 958
- Vrba, F. J., Coyne, G. V., & Tapia, S. 1981, *ApJ*, 243, 489
- Vrba, F. J., & Rydgren, A. E. 1985, *AJ*, 90, 1490
- Vrba F. J., Marraco, H. G., & Strom, S. E., 1992, *BAAS*, 24, 1246
- Vrba, F. J., Coyne, G. V., & Tapia, S. 1993, *AJ*, 105, 1010
- Wardle, M. 1998, *MNRAS*, 298, 507
- Whittet, D. C. B. 1992, *Dust in the Galactic Environment* (Philadelphia: Inst. Phys.. Publ.)
- Whittet, D. C. B., Gerakines, P. A., Carkner, A. L., Hough, J. H., Martin, P. G., Prusti, T., & Kilkenny, D. 1994, *MNRAS*, 268, 1
- Whittet, D. C. B., Gerakines, P. A., Hough, J. H., & Shenoy, S. S. 2001, *ApJ*, 547, 872
- Woermann, B., Gaylard, M. J., & Otrupcek, R. 2001, *MNRAS*, 325, 1213
- Williams, R. J. R., Dyson, J. E., & Hartquist, T. W. 2000, *MNRAS*, 314, 315
- Williams, R. J. R., & Dyson, J. E. 2001, *MNRAS*, 325, 293
- Zweibel, E. G. 1990, *ApJ*, 362, 545